

# Probing the strongly driven spin-boson model in a superconducting quantum circuit

L. Magazzù<sup>†,1</sup> P. Forn-Díaz<sup>†,2,3,4,5</sup> R. Belyansky<sup>2,6</sup> J.-L. Orgiazzi<sup>2,4,6</sup> M. A. Yurtalan<sup>2,4,6</sup> M. R. Otto<sup>2,3,4</sup> A. Lupascu<sup>\*,⊥,2,3,4</sup> C. M. Wilson<sup>\*,⊥,2,6</sup> and M. Grifoni<sup>\*7</sup>

<sup>1</sup>*Institute of Physics, University of Augsburg,*

*Universitätsstraße 1, D-86135 Augsburg, Germany*

<sup>2</sup>*Institute for Quantum Computing, University of Waterloo, Waterloo N2L 3G1, Canada*

<sup>3</sup>*Department of Physics and Astronomy,*

*University of Waterloo, Waterloo N2L 3G1, Canada*

<sup>4</sup>*Waterloo Institute for Nanotechnology,*

*University of Waterloo, Waterloo N2L 3G1, Canada*

<sup>5</sup>*Barcelona Supercomputing Center (BSC),*

*C/ Jordi Girona 29, 08034 Barcelona, Spain*

<sup>6</sup>*Department of Electrical and Computer Engineering,*

*University of Waterloo, Waterloo N2L 3G1, Canada*

<sup>7</sup>*Institute for Theoretical Physics, University of Regensburg, 93040 Regensburg, Germany*

(Dated: February 22, 2023)

Quantum two-level systems interacting with the surroundings are ubiquitous in nature. The interaction suppresses quantum coherence and forces the system towards a steady state. Such dissipative processes are captured by the paradigmatic spin-boson model, describing a two-state particle, the “spin”, interacting with an environment formed by harmonic oscillators. A fundamental question to date is to what extent intense coherent driving impacts a strongly dissipative system. Here

---

† These authors contributed equally to this work.

⊥ The experimental work was a collaboration between the labs led by these researchers.

\* adrian.lupascu@uwaterloo.ca; chris.wilson@uwaterloo.ca; milena.grifoni@ur.de;

we investigate experimentally and theoretically a superconducting qubit strongly coupled to an electromagnetic environment and subjected to a coherent drive. This setup realizes the driven Ohmic spin-boson model. We show that the drive reinforces environmental suppression of quantum coherence, and that a coherent-to-incoherent transition can be achieved by tuning the drive amplitude. An out-of-equilibrium detailed balance relation is demonstrated. These results advance fundamental understanding of open quantum systems and bear potential for applications in quantum technologies.

The spin-boson model has been prominent for several decades in the study of open quantum systems [1, 2]. It describes the simplest quantum system, a two-state system (spin), interacting with its environment. The latter is modeled as a set of harmonic oscillators (bosons) constituting a so-called heat bath. The dynamical regimes of the spin-boson model at a given finite temperature are essentially dictated by the coupling to the environment and by the low-frequency behavior of the bath spectrum. In the strong coupling regime, this model provides an accurate representation of a variety of physical and chemical situations of broad interest, including incoherent tunneling of bistable defects in metals [3] and amorphous systems [4], macroscopic quantum tunneling in superconducting circuits [5], or electron and proton transfer in solvent environments [6]. The weak coupling regime is relevant in situations where preserving quantum coherence is crucial, such as in quantum computing, whereas strong coupling is important for applications relying on the transfer of information between the system and the environment, as needed in quantum communication.

In the Ohmic spin-boson model, the environment has a linear spectrum at low frequencies which leads to various remarkable phenomena, such as bath-induced localization or a coherent-to-incoherent transition even at zero temperature for large enough coupling strengths [2].

Recently, a new experimental system was realized [7] which is described by the Ohmic

spin-boson model with an environmental coupling tunable from weak to ultrastrong [8]. This particular implementation is formed from a superconducting flux qubit coupled to a transmission line, which play the role of the two-state system and environment, respectively. The tunability of the interaction allows one to test the key predictions of the spin-boson model. In [9], a qubit ultrastrongly coupled to a single oscillator mode was demonstrated.

In this article, we study the spin-boson setup from Ref. [7] under strong driving, which adds a new dimension of exploration for a spin-boson system [3]. Previous experiments studying strongly driven systems have reported remarkable effects, such as the formation of dressed states [11–13], Landau-Zener interference [14, 15], amplitude spectroscopy [16], and the observation of Floquet states [17]. However, these experimental reports were restricted to weak or moderate coupling to the environment. Here, for the first time, we combine intense driving and diverse dissipation strengths in a superconducting qubit circuit, with the aim of tracing out the dynamical phase diagram of a driven spin-boson particle at strong coupling.

A schematic representation of the experimental setup is shown in Fig. 1(a). The two-state system is a superconducting circuit consisting of a loop interrupted by four Josephson junctions, a so-called flux qubit [18]. The bosonic environment is formed from electromagnetic modes in the superconducting transmission line coupled to the qubit. The qubit is pumped by a strong continuous-wave drive applied through the transmission line. Both the amplitude and the frequency of the drive can be changed over a broad range. The driven system is studied spectroscopically by additionally applying a weak *probe* field. The measured transmission at the probe frequency gives direct access to the linear response function associated with the weak probe signal, the so-called linear susceptibility  $\chi$ . The latter fully characterizes the dynamical phases of the driven spin-boson system. By measuring the transmission also when the drive is switched off, we get a reference for the effects of a coherent drive on quantum coherence and localization properties.

We first introduce the spin-boson model and its dynamics without driving. Histori-

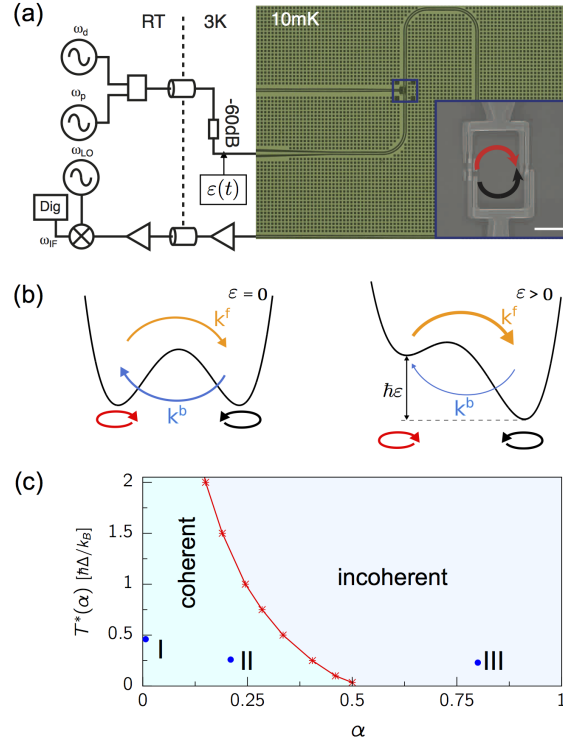


FIG. 1. **Experimental setup and phase diagram of the symmetric spin-boson model.**

**a**, Measurement, driving circuit schematic and optical micrograph of a device similar to the ones used in the experiment. A coplanar waveguide running across the chip plays the role of the bath coupled to the qubit. The inset is a scanning electron micrograph showing the qubit attached to the line. The scale bar is 2  $\mu\text{m}$ . Here and in panel **(b)** the red (black) arrow indicates clockwise (anticlockwise) circulating persistent currents. **b**, Schematics of the double-well potential associated with the flux threading the qubit. In the absence of external driving sources the potential is symmetric and the forward and backward tunneling rates  $k^f/b$  are equal. In the presence of a positive bias asymmetry  $\varepsilon$ , forward tunneling dominates over backward tunneling. **c**, Dependence of the temperature  $T^*(\alpha)$  for the crossover from the coherent to the incoherent tunneling regime on the coupling  $\alpha$ . The red curve interpolates numerical results (asterisks) obtained within the nonperturbative NIBA.

cally, the Ohmic spin-boson model was first studied in the context of the tunneling of a quantum particle in a double-well potential [2]. At low temperatures the dynamics are effectively restricted to the Hilbert space spanned by the states  $|L\rangle$  and  $|R\rangle$ , localized in the left and right well, respectively [see Fig. 1(b)]. Transitions between the two localized configurations are possible due to quantum-mechanical tunneling and are recorded in the time evolution of the population difference  $P(t) \equiv \langle \sigma_z(t) \rangle = P_R(t) - P_L(t)$  of the two localized eigenstates. The coordinate associated with the double-well potential need not to be geometrical, but it can represent other continuous variables. For the superconducting flux qubit used in our experiment, this is the magnetic flux  $\Phi$  in the loop. The eigenstates  $|L\rangle$  and  $|R\rangle$  of the flux operator are related to currents circulating clockwise/anticlockwise in the superconducting loop [18] [see red/black arrows in Figs. 1(a,b)]. In this basis, the qubit Hamiltonian is

$$H_{\text{qb}}(t) = -\frac{\hbar}{2} [\Delta \sigma_x + \varepsilon(t) \sigma_z] , \quad (1)$$

where  $\sigma_i$  are the Pauli matrices. The parameter  $\Delta$  accounts for interwell tunneling and  $\hbar\varepsilon(t)$  is the difference in energy between the two wells, which is controllable. The electromagnetic field in the transmission line can be described as a continuously distributed set of propagating modes with a distribution in frequency given by the spectral density

$$G(\omega) = 2\alpha\omega e^{-\omega/\omega_c} , \quad (2)$$

corresponding to Ohmic damping with the dimensionless coupling strength  $\alpha$  and high frequency cutoff  $\omega_c$ .

Theoretical work on the spin-boson model has primarily focused on the temporal dynamics of the spin. Quite generally, independent of the initial state of the qubit and the form of the bath spectral density, energy exchange with the environment is responsible for equilibration of the qubit with the bath on a time scale given by the relaxation time  $T_1 = 1/\gamma_r$ . The relaxation rate  $\gamma_r = k^f + k^b$  accounts for forward/backward tunneling transitions between the localized states accompanying relaxation [see Fig. 1(b)]. Furthermore, quantum fluctuations and energy exchange yield dephasing on a time scale

$T_2 = 1/\gamma$ , where  $\gamma$  is the dephasing rate. In the Ohmic spin-boson model, low frequency environmental modes also lead to a strong renormalization of the bare qubit tunneling splitting  $\Delta$ . The renormalized qubit frequency  $\Omega$  depends on the bath temperature and coupling strength  $\alpha$ , and is always reduced with respect to  $\Delta$ . This leads to three distinct dynamical regimes. Two of them, occurring for  $\alpha < 1$ , are depicted in Fig. 1(c) for the symmetric spin-boson model shown in the left drawing in Fig. 1(b). The coherent regime corresponds to  $\Omega > \gamma$ . This occurs for  $\alpha < 1/2$  and a temperature  $T < T^*(\alpha)$ . In this regime, for a spin initially localized in the right well ( $P(0) = 1$ ), the qubit displays damped coherent oscillations of frequency  $\Omega$ , specifically,  $P(t) = \exp(-\gamma t) \cos(\Omega t)$  [see insets of Fig. 2(a,b)]. At the crossover temperature, the renormalized frequency  $\Omega$  vanishes (see Methods and Eq. (20) there). The incoherent regime corresponds to  $\alpha < 1/2$  and  $T > T^*(\alpha)$  or  $1/2 < \alpha < 1$ . The dynamics are characterized by incoherent tunneling transitions with rates  $k^{f/b}$ . Correspondingly we have  $P(t) = e^{-\gamma t}$  [see inset in Fig. 2(c)]. In the third regime, corresponding to  $\alpha > 1$ , localization occurs. Here, the backward and forward rates are renormalized to zero by the low-frequency bath modes.

The primary scope of this work is to understand how the dynamical phase diagram in Fig. 1(c) is modified by a strong coherent drive. To this aim, we use a spectroscopic approach where the bias between the wells in our experimental setup is described by

$$\varepsilon(t) = \varepsilon_0 + \varepsilon_p \cos(\omega_p t) + \varepsilon_d \cos(\omega_d t) . \quad (3)$$

Here, the static component  $\varepsilon_0$  is related to the externally applied flux  $\Phi_\varepsilon$  by  $\varepsilon_0 \propto (\Phi_\varepsilon - \Phi_0/2)$ , with  $\Phi_0$  the magnetic flux quantum. The remaining contributions account for the probe (p), with amplitude  $\varepsilon_p$  and frequency  $\omega_p$ , and the drive (d), with amplitude  $\varepsilon_d$  and frequency  $\omega_d$ . For details, see the Methods. The central quantity in this work is the linear susceptibility  $\chi(\omega_p)$ , which describes the qubit's response at the probe frequency  $\omega_p$ . The susceptibility measures deviations of the steady state population difference,  $P^{\text{st}}(t)$ , from its value  $P_0$  in the absence of the weak probe according to [5]

$$P^{\text{st}}(t) = P_0 + \hbar \varepsilon_p [\chi(\omega_p) e^{i\omega_p t} + \chi(-\omega_p) e^{-i\omega_p t}] . \quad (4)$$

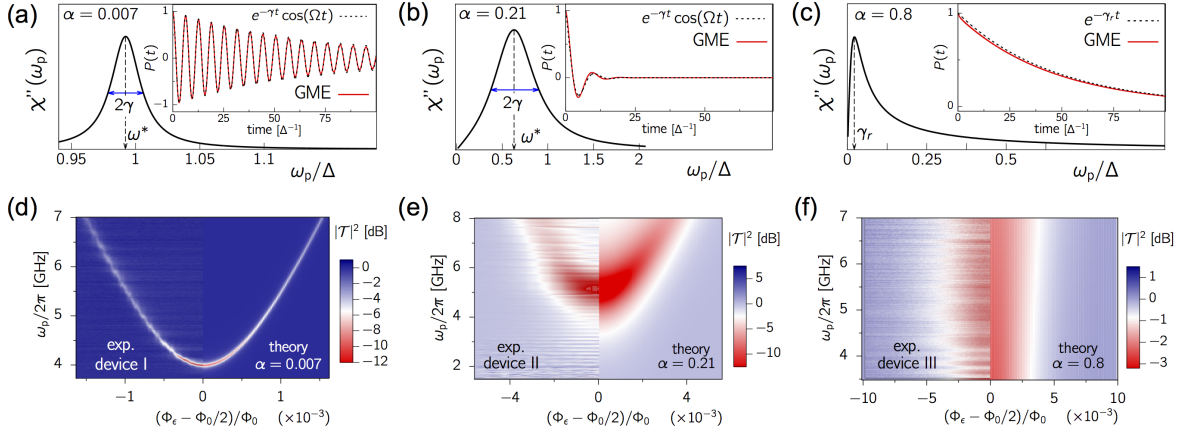


FIG. 2. **Spin-boson dynamics and spectra at different coupling strengths in the absence of the drive.** **a-c**, Frequency dependence of the imaginary part  $\chi''(\omega_p)$  of the linear susceptibility and time evolution of the population difference  $P(t)$  (insets) for the three selected combinations of coupling and temperature shown in Fig. 1(c). The position  $\omega^*$  and FWHM  $2\gamma$  of the linear susceptibility peak in the coherent regimes ( $\alpha = 0.007$ ,  $\alpha = 0.21$ ) provide a direct measure of the renormalized qubit frequency  $\Omega = \sqrt{(\omega^*)^2 - \gamma^2}$ . In the incoherent regime ( $\alpha = 0.8$ ), the peak position yields the relaxation rate  $\gamma_r$ . **d-f**, Experimental transmission spectra of three flux qubit devices with different coupling junctions are compared with spectra calculated within the NIBA. The characteristic hyperbolic spectrum of the flux qubit is evident in (d) and recognizable in (e). Its disappearance in (f) indicates the transition to the incoherent regime. At  $\Phi_\epsilon = \Phi_0/2$  the spin-boson system is unbiased, which is the situation of panels (a-d).

On the one hand, according to Kubo's linear response theory [20],  $\chi(\omega)$  carries information about the dispersive and absorptive properties of the qubit in the *absence* of the probe, and hence about the driven, dissipative qubit dynamics. On the other hand, the linear susceptibility is directly accessible by measuring the transmitted probe amplitude  $\mathcal{T}(\omega_p)$  via the relation

$$\mathcal{T}(\omega_p) = 1 - i\mathcal{N}\hbar\omega_p\chi(\omega_p), \quad (5)$$

where  $\mathcal{N}$  is a coupling constant (see Methods). In this work, the dynamical quantities  $P(t)$

and  $\chi(\omega_p)$  have been calculated within the so-called noninteracting-blip approximation (NIBA). This approximation yields a generalized master equation for  $P(t)$  with kernels that are nonperturbative in  $\alpha$ . It becomes exact at large temperatures and/or coupling strengths [1]. Under the assumption that  $\omega_d$  is large compared to the (renormalized) frequency scales of the spin-boson particle, closed expressions for the transient evolution of  $P(t)$ , as well as for the linear susceptibility of the driven spin-boson system, can be obtained (details in the Methods).

We first demonstrate in Figs. 2(a-c) the connection between the imaginary part,  $\chi''(\omega_p)$ , of the susceptibility and  $P(t)$  for the symmetric spin-boson model in the presence of the probe only ( $\varepsilon_0 = \varepsilon_d = 0$ ). We choose three distinct values of the coupling, namely  $\alpha = 0.007, 0.21$ , situated in the coherent regime, and  $\alpha = 0.8$  in the incoherent regime (see the three dots indicated in Fig. 1(c)). In the coherent regime,  $\chi''(\omega_p)$  has a peak at  $\omega^* = (\Omega^2 + \gamma^2)^{1/2}$  with full width at half maximum (FWHM) given by  $2\gamma$ . In the incoherent regime, the peak is located near zero frequency, at the value of the relaxation rate  $\gamma_r$ . According to Eq. (IB), a maximum in  $\chi''(\omega_p)$  corresponds to a minimum in the transmission  $\mathcal{T}(\omega_p)$ . By recording the evolution of the transmission as a function of  $\omega_p$  and of another external parameter, e.g. the static asymmetry  $\varepsilon_0$ , various dynamical regimes can be identified.

The theoretically calculated transmission is presented in Figs. 2(d-f) (right panels) as a function of the applied static bias  $\varepsilon_0$  for the three values of  $\alpha$  discussed above. As expected, the qubit dispersion relation can be traced back in the highly coherent and underdamped regimes corresponding to  $\alpha = 0.007$  and  $\alpha = 0.21$ . In the overdamped regime with  $\alpha = 0.8$  the transmission is independent of  $\omega_p$ . Finally, comparison with the measured transmission (left panels) for three distinct devices, named I, II and III, in the following, allows us to position the three devices as shown in the phase diagram in Fig. 1(c) [21]. The close agreement between the calculated and measured qubit spectra gives a strong evidence that device III is in the nonperturbative ultrastrong coupling regime, buttressing the conclusion of [7, 22]. In a recent work [23] a polaron approach,

which is equivalent to the NIBA [1], has been used to provide approximate expressions for the response of an undriven qubit coupled to a transmission line.

Let us now turn to the impact of a strong coherent drive on a spin-boson particle in the

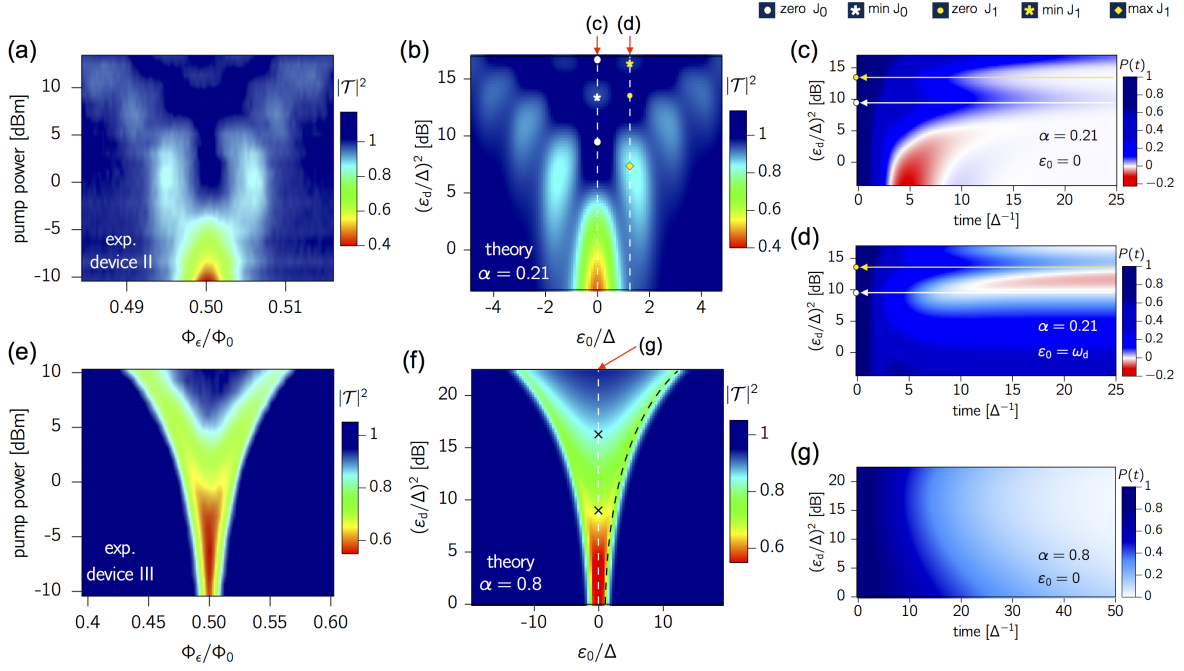


**FIG. 3. Spectral response and dynamics of the driven spin-boson system.** **a** Observed transmission at the probe frequency for the moderately coupled device II as function of static bias and pump strength. A clear structure of multi-photon resonances appears at large driving powers. **b** Theory prediction in the same dissipation ( $\alpha = 0.21$ ) and driving regimes as in (a). Dashed lines indicate cuts at fixed bias where panels (c) and (d) are calculated. **c, d** Predicted dynamics of  $P(t)$  with  $P(0) = 1$ . **e, f** Observed and calculated spectrum of the ultrastrongly coupled device III (corresponding to  $\alpha = 0.8$ ). The spectrum is smoothed compared to panels (a), (b) and indicates a fully incoherent dynamics. The black dashed line corresponds to the condition  $\varepsilon_{\text{eff}} = 2k_{\text{B}}T/\hbar$  for the effective nonequilibrium bias. **g** Time evolution of  $P(t)$  calculated at the symmetry point,  $\varepsilon_0 = 0$ , in the same range of pump strengths as in panel (f).

intermediate and ultrastrong coupling regimes captured by devices II and III, respectively.

The experimental spectra in Figs. 3(a,e) show the probe transmission as a function of flux bias  $\varepsilon_0$  and drive power ( $\propto \varepsilon_d^2$ ) for these devices. Probe and drive frequencies are respectively set to  $\omega_p/2\pi = 5.2$  GHz and  $\omega_d/2\pi = 9$  GHz for device II. For device III we choose  $\omega_p/2\pi = 4$  GHz and  $\omega_d/2\pi = 3$  GHz. For device II, the probe is on-resonance with the undriven qubit. For device III, the qualitative features of the driven spectra are largely insensitive to the choice of  $\omega_p$  and  $\omega_d$ . The theoretical predictions, shown in Figs. 3(b,f), agree well with the experimental observations. Similar to the pump-only case, striking differences are observed in the transmission of the two devices. Let us start discussing device II. Minima in the transmission are clearly seen in Figs. 3(a,b) whenever the static bias matches a multiple of the pump frequency,  $\varepsilon_0 = n\omega_d$ , as indicated by the vertical lines drawn in Fig. 3(b) for  $n = 0, 1$ . Furthermore, the observed pattern with fixed bias at the  $n$ -th resonance results from a modulation by a prefactor proportional to  $J_n(\varepsilon_d/\omega_d)$ , where  $J_n$  is a Bessel function of the first kind. For example, the qubit response at the symmetry point is suppressed in correspondence with the first zero of the Bessel function  $J_0(\varepsilon_d/\omega_d)$  (indicated by a circle), where the incoming probing field is fully transmitted. At larger power, as the zero order Bessel function increases again, the transmission diminishes. Similar patterns have already been reported in driven qubit devices in the highly coherent regime [12, 15]. Those results can be interpreted as a signature of entangled light-matter states known as dressed-states [11, 24, 25]. Near the multiphoton resonance,  $\varepsilon_0 = n\omega_d$ , two of these dressed states form an effective two-level system with dressed tunneling splitting  $\Delta_n = \Delta J_n(\varepsilon_d/\omega_d)$ . Near a zero of the  $n$ -th Bessel function, tunneling is strongly suppressed and hence the transmission is maximal. This phenomenon has been dubbed coherent destruction of tunneling in the literature [26]. Dissipation modifies this simple coherent picture, as demonstrated for device III in Figs. 3(e,f) where no Bessel pattern is present and a smooth “V-shaped” transmission is observed instead.

To understand to what extent dissipation modifies the dressed state picture, we have studied the transient dynamics of the population  $P(t)$  in the presence of drive only ( $\varepsilon_p = 0$ ). By solving the pole equation  $\lambda + K^+(\lambda) = 0$ , the phase diagram of the

driven spin-boson particle can be found along the lines discussed in the Methods. Here,  $K^+(\lambda) = K^f(\lambda) + K^b(\lambda)$  is the sum of the nonequilibrium kernels for forward and backward tunneling

$$K^{f/b}(\lambda) = \frac{\Delta^2}{2} \int_0^\infty dt e^{-Q'(t)-\lambda t} J_0[d(t)] \cos[Q''(t) \mp \varepsilon_0 t], \quad (6)$$

with  $d(t) = \frac{2\varepsilon_d}{\omega_d} \sin\left(\frac{\omega_d t}{2}\right)$ . The correlation function  $Q(t) = Q'(t) + iQ''(t)$  describes the environmental influence and its explicit form is discussed in the Supplement and in Eq. (29) of the Methods. For the present discussion, it is enough to observe that in the long-time limit  $t \gg \tau_{\text{env}}$ , where  $\tau_{\text{env}} = (2\pi\alpha k_B T/\hbar)^{-1}$ , the real part of  $Q(t)$  assumes the form  $Q'(t) \sim t/\tau_{\text{env}} + \text{const.}$  appropriate to white noise. Thus,  $\tau_{\text{env}}$  yields an estimate of the memory time of the kernels entering Eq. (6). The impact of the drive is encapsulated in the time-dependent argument of the Bessel function of first kind  $J_0$ . Depending on whether  $\omega_d \tau_{\text{env}} \geq 1$  or  $\omega_d \tau_{\text{env}} \leq 1$ , two distinct regimes corresponding to devices II and III are encountered, respectively. Let us focus on the first case, explored in Figs. 3(a-b). In this regime, one full cycle of the drive field is possible before environmental effects induce a loss of coherence. Thus, we expect that coherent absorption and emission processes from the drive field take place during a cycle. An expansion of the Bessel function in Eq. (6) in a Fourier series,  $J_0[d(t)] = \sum_n J_n^2(\varepsilon_d/\omega_d) \exp(in\omega_d t)$ , shows that the channel with  $n\omega_d = \varepsilon_0$  dominates the series [3], and hence an effective two-level description with renormalized tunneling splitting  $\Delta_n$  applies. A solution of the pole equation in this approximation yields a renormalization of the crossover temperature  $T^*(\alpha) \rightarrow T^*(\alpha)[J_n(\varepsilon_d/\omega_d)]^{1/(1-\alpha)}$ . Because  $J_n < 1$ , the pump field always yields a *reduction* of quantum coherence. Near the zeros of  $J_n$  quantum coherence is *fully suppressed* and an incoherent decay is expected. This behavior is seen in Figs. 3(c,d), where we show the simulated time evolution of  $P(t)$  as a function of pump power at  $\varepsilon_0 = 0$  and  $\varepsilon_0 = \omega_d$ , respectively. The color map of  $P(t)$  displays coherent oscillations at low to moderate pump amplitudes, where  $J_0(\varepsilon_d/\omega_d)$  is still of order one. However, a full suppression of quantum coherence occurs near the first zero of  $J_0$ , highlighted by a solid white circle. We notice that the almost complete standstill predicted to occur at the zeros of  $J_0$  for a dissipation-free, symmetric two-level particle

[26], is destroyed by environmental relaxation processes, albeit on a very slow time scale. A similar suppression of coherence, together with a very slow relaxation, is observed at the first resonance,  $\varepsilon_0 = \omega_d$ , shown in Fig. 3(d), in correspondence with the first zero of  $J_1$ . Independently of the initial preparation, the steady state population acquires the value  $P_0 = (K^f - K^b)/(K^f + K^b)$ , where  $K^{f/b} = K^{f/b}(\lambda = 0)$  are the nonequilibrium backward and forward rates. For the symmetric case shown in Fig. 3(c), the backward and forward rates are equal and hence  $P_0 = 0$ . A genuine nonequilibrium behavior is observed in Fig. 3(d) in the region between the first zeros of  $J_0$  and  $J_1$ , where the steady state qubit population  $P_0 < 0$ , corresponding to a larger population of the left state despite  $\varepsilon_0 > 0$ . This phenomenon originates from the effective detailed balance relation

$$K^f = K^b e^{\hbar\varepsilon_{\text{eff}}/k_B T} \quad (7)$$

between the nonequilibrium backward and forward rates  $K^{f/b}$ , with the effective asymmetry  $\varepsilon_{\text{eff}}$  defined implicitly through Eq. (6). Only in the absence of the drive does  $\varepsilon_{\text{eff}}$  coincide with the static bias  $\varepsilon_0$ . We note that the use of an external coherent drive to tune the direction of long-range electron chemical reactions was originally proposed in [27, 28].

Let us turn to the explanation of the results for device III displayed in Figs. 3(e-g), where  $\omega_d \tau_{\text{env}} \ll 1$  applies. In this regime the approximate result

$$\chi(\omega_p) = \frac{1}{4k_B T} \frac{\partial \varepsilon_{\text{eff}} / \partial \varepsilon_0}{\cosh^2(\hbar\varepsilon_{\text{eff}}/2k_B T)} \frac{\gamma_d}{\gamma_d + i\omega_p} \quad (8)$$

can be obtained from the exact expression Eq. (16) of the Methods. This form is associated with incoherent dynamics of the spin boson particle with nonequilibrium relaxation rate  $\gamma_d \equiv K^f + K^b$ . At the symmetry point,  $\varepsilon_{\text{eff}} = \varepsilon_0 = 0$  and  $\lim_{\varepsilon_0 \rightarrow 0} \partial \varepsilon_{\text{eff}} / \partial \varepsilon_0 \neq 0$ . Correspondingly, the susceptibility  $\chi''(\omega_p)$  has a peak at  $\omega_p = \gamma_d$ . An expansion in the small parameter  $\omega_d \tau_{\text{env}}$  yields  $J_0[d(t)] \approx J_0(\varepsilon_d t)$  and hence a relaxation rate,  $\gamma_d$ , independent of the driving frequency  $\omega_d$ , which is consistent with the experimental observation that the spectra depend weakly on  $\omega_d$ . The dependence on the pump amplitude  $\varepsilon_d$  remains. This is clearly seen in Figs. 3(e-g) in the smooth increase of the transmission at the symmetry

point as the drive amplitude is increased. The transmission is almost complete for drive powers above the value  $(\varepsilon_d/\Delta)^2 \simeq 16$  dB roughly corresponding to the second zero of  $J_0(\varepsilon_d\tau_{\text{env}})$  (see Fig. 3(f), where the black crosses highlight the first two zeroes). Regarding the transmission at finite static bias, we expect that no thermally assisted excitation is possible when  $\hbar\varepsilon_{\text{eff}} \gg k_B T$ ; correspondingly the susceptibility vanishes, as accounted by the term  $\cosh^{-2}(\hbar\varepsilon_{\text{eff}}/2k_B T)$  in Eq. (8). This behavior is clearly seen in Fig. 3(f), where the black dashed line corresponds to the condition  $\hbar\varepsilon_{\text{eff}} = 2k_B T$ . Below the dashed line the effective bias is larger than the temperature and the signal is fully transmitted.

In conclusion, we have experimentally and theoretically explored the paradigmatic driven spin-boson model in the underdamped and overdamped dynamical regimes. Quantum coherence is generally reduced or even destroyed by a drive field in a way which can be tuned by sweeping the drive amplitude and frequency. The control of the dynamics is possible for a generic Ohmic spin-boson particle, independently of its microscopic details. Localization and even population inversion can be attained by properly tuning the parameters of the coherent drive. Besides having an important fundamental interest, our findings may have far-reaching impact in the attempt to tune the performance of quantum devices and engineering quantum environments for physical and chemical applications.

## Methods

### Experimental fabrication

Devices were fabricated according to the procedure explained in Ref. [7].

### Relation between theoretical and experimental observables

The flux operator in the qubit basis is identified with  $\hat{\Phi} = f\sigma_z$ . The proportionality constant  $f$  is a fitting parameter which, for low couplings, is estimated to be  $f = MI_p$ , with  $M$  the qubit-line mutual inductance and  $I_p$  the persistent current in the superconducting loop. This estimate provides values (see Table 1) which are not far from those obtained

from fit to data for devices I and II and from qualitative analysis for device III. The externally applied tunable flux  $\Phi_\epsilon$  is related to the static bias by  $\hbar\epsilon_0 = 2I_p(\Phi_\epsilon - \Phi_0/2)$ , with  $\Phi_0$  the magnetic flux quantum. The probe input voltage is connected to the angular frequency  $\epsilon_p$  yielding the theoretical probe amplitude, see Eq. (3), through  $V_p^{\text{in}}(t) = f_Z \epsilon_p \cos(\omega_p t)$ , where the proportionality constant is  $f_Z = \hbar Z/f$  and  $Z$  is the line impedance. It follows that the constant  $\mathcal{N}$  in Eq. (IB) is given by the ratio  $f/f_Z$ .

### Parameters used in the simulation

The parameters used in the numerical simulations shown in Figs. 2, 3 are provided in the Table 1. Coupling  $\alpha$ , bare tunneling frequency  $\Delta$ , and proportionality constant  $\mathcal{N}$  are determined by fit to data of  $|\mathcal{T}|^2$  vs  $\omega_p$  performed for the nondriven devices I and II at the symmetry point  $\Phi_\epsilon = \Phi_0/2$  [see Fig. 2(d-e)]. In Fig. 2, the measured value of 90 mK is used for the temperature. Temperature values used in Fig. 3 account for a possibly higher effective temperature introduced by the drive at the qubit position. Specifically, for device II, in the presence of the pump drive, a better qualitative agreement between simulated and experimental transmission is obtained by assuming a higher temperature. As the qualitative features of the simulated transmission for device III, operating at ultrastrong coupling, are weakly sensitive to variations of the temperature, we used the same value of temperature for the pump-probe and the probe-only cases.

### Theoretical methods

#### *I. Spin-boson Hamiltonian*

The spin-boson model describes the coupling of a two-level quantum system to a bath of harmonic oscillators [29]. By assuming a coupling which linearly depends on the coordinates of the oscillators, one arrives at the famous spin-boson Hamiltonian

$$H(t) = H_{\text{qb}}(t) - \frac{\hbar}{2} \sigma_z \sum_i c_i (a_i^\dagger + a_i) + \sum_i \hbar \omega_i a_i^\dagger a_i, \quad (9)$$

where  $a_i, a_i^\dagger$  are bosonic annihilation and creation operators and the coefficients  $c_i$  are the amplitude of the interaction strength of the two-level system with mode  $i$ . The bosonic

**Table 1. Parameters used for simulations**

<b>Fig. 2 &amp; 3</b>	<i>Device I</i>	<i>Device II</i>	<i>Device III</i>
$\omega_c/2\pi$ (GHz)	65	65	65
$I_p$ (nA)	600	280	250
$\alpha$	0.007 [fit]	0.21 [fit]	0.8*
$\Delta/2\pi$ (GHz)	4.04 [fit]	7.23 [fit]	8.0*
<b>Fig. 2</b>	<i>Device I</i>	<i>Device II</i>	<i>Device III</i>
$T$ (mK)	90	90	90
$\mathcal{N}$ (estimated)	0.03 [fit] (0.02)	1.1 [fit] (0.5)	8.0* (5 – 10)
<b>Fig. 3</b>		<i>Device II</i>	<i>Device III</i>
$T$ (mK)		175*	90*
$\mathcal{N}$		1.1*	16.0*
$\omega_p/2\pi$ (GHz)		5.2	4.0
$\omega_d/2\pi$ (GHz)		9.0	3.0

\*value yielding qualitative agreement with the experiment.

heat bath is fully characterized by the spectral function  $G(\omega) = \sum_i c_i^2 \delta(\omega - \omega_i)$ . For Ohmic damping,  $G(\omega) \propto \omega$ , as assumed in Eq. (2).

## II. Driven spin-boson dynamics within the NIBA.

The Ohmic spin-boson problem owes its popularity to its ubiquity and to the variety of parameter regimes it encompasses as the temperature  $T$  and the coupling strength  $\alpha$  are varied. We refer the readers to Ref. [1] for an exhaustive treatment. The dynamical properties of a driven spin-boson system in the strongly damped and in the incoherent regimes, are well described within the so-called noninteracting-blip approximation (NIBA). Furthermore, the NIBA captures well the dynamics of a symmetric ( $\varepsilon_0 = 0$ ) spin-boson system in the whole parameter regime. The NIBA approximation provides a generalized

master equation (GME) for the evolution of the population difference  $P(t)$  with rates in second order in the bare tunneling splitting  $\Delta$  but nonperturbative in  $\alpha$ . Accounting for the presence of time dependent fields, the GME explicitly reads

$$\dot{P}(t) = \int_{t_0}^t dt' [\mathcal{K}^-(t, t') - \mathcal{K}^+(t, t')P(t')]. \quad (10)$$

The NIBA kernels  $\mathcal{K}^\pm$ , averaged over a pump period, are given by

$$\begin{aligned} \mathcal{K}^+(t, t') &= h^+(t - t') \cos[\zeta(t, t')], \\ \mathcal{K}^-(t, t') &= h^-(t - t') \sin[\zeta(t, t')], \end{aligned} \quad (11)$$

with

$$\begin{aligned} h^+(t) &= \Delta^2 e^{-Q'(t)} \cos[Q''(t)] J_0 \left[ \frac{2\varepsilon_d}{\omega_d} \sin\left(\frac{\omega_d t}{2}\right) \right], \\ h^-(t) &= \Delta^2 e^{-Q'(t)} \sin[Q''(t)] J_0 \left[ \frac{2\varepsilon_d}{\omega_d} \sin\left(\frac{\omega_d t}{2}\right) \right]. \end{aligned} \quad (12)$$

The function  $Q(t) = Q'(t) + iQ''(t)$  is the environmental correlation function. For the Ohmic spectral density function  $G(\omega) = 2\alpha\omega \exp(-\omega/\omega_c)$ ,  $\alpha$  being the dimensionless coupling strength and  $\omega_c$  a high frequency cutoff, and in the scaling limit  $\hbar\omega_c \gg \beta^{-1} = k_B T$ , these functions have an explicit form [1]

$$\begin{aligned} Q'(t) &= 2\alpha \ln \left[ \sqrt{1 + \omega_c^2 t^2} \frac{\sinh(\pi t/\hbar\beta)}{\pi t/\hbar\beta} \right], \\ Q''(t) &= 2\alpha \arctan(\omega_c t). \end{aligned} \quad (13)$$

The above formulas are accurate in all coupling regimes, provided that the cutoff frequency is large with respect to the other frequency scales involved. In the long-time limit ( $t/\beta\hbar \gg 1$ ) the real part of  $Q(t)$  assumes the form  $Q'(t) \sim t/\tau_{\text{env}} + \text{const.}$ , where  $\tau_{\text{env}} = (2\pi\alpha k_B T/\hbar)^{-1}$ . Thus the latter quantity determines the memory time of the kernels  $\mathcal{K}^\pm$ , Eq. (23).

The dynamical phase, entering the kernels in Eq. (23), reads

$$\zeta(t, t') = (t - t')\varepsilon_0 + \frac{\varepsilon_p}{\omega_p} \{\sin(\omega_p t) - \sin[\omega_p(t')]\}. \quad (14)$$

Note that in the absence of the probe field,  $\varepsilon_p = 0$ , the pump-averaged kernels depend only on the difference  $t - t'$ , i.e.,  $\mathcal{K}^\pm(t, t') = \mathcal{K}^\pm(t - t')$ , as in the static case. The latter is then recovered by additionally setting  $\varepsilon_d = 0$ . On the other hand, the probe-only setup is described by Eq. (10) upon setting  $\varepsilon_d = 0$  in Eq. (12). The dynamics shown in the insets of Figs. 2(a-c) are based on the numerical solution of the GME (10) for  $\varepsilon(t) = 0$ , whereas in the time evolution of  $P(t)$  vs. pump power shown in panels (c), (d), and (g) of Fig. 3, only the probe field is set to zero.

### III. The linear susceptibility

The linear susceptibility is related to the stationary probability difference by

$$P^{\text{st}}(t) = P_0 + \hbar\varepsilon_p[\chi(\omega_p)e^{i\omega_p t} + \chi(-\omega_p)e^{-i\omega_p t}], \quad (15)$$

where, in the NIBA,  $P_0$  reduces to the equilibrium value  $P_{\text{eq}} = \tanh(\hbar\varepsilon_0/2k_B T)$  in the absence of pump driving. The transmission  $\mathcal{T}(\omega_p)$  and the susceptibility  $\chi(\omega_p)$  shown in the theoretical plots of Figs. 2 and 3 are calculated by means of the exact NIBA expression [3]

$$P_0 = \frac{K^-(0)}{K^+(0)}, \quad \chi(\omega_p) = \frac{H^+(\omega_p) - H^-(\omega_p)P_0}{i\omega_p + K^+(i\omega_p)}, \quad (16)$$

with superscripts  $\pm$  denoting symmetric/antisymmetric functions of  $\varepsilon_0$ . For our pump-probe case we find

$$\begin{aligned} H^+(\omega_p) &= \frac{1}{\hbar\omega_p} \int_0^\infty dt e^{-i\omega_p t/2} \sin\left(\frac{\omega_p t}{2}\right) h^-(t) \cos(\varepsilon_0 t) \\ H^-(\omega_p) &= \frac{-1}{\hbar\omega_p} \int_0^\infty dt e^{-i\omega_p t/2} \sin\left(\frac{\omega_p t}{2}\right) h^+(t) \sin(\varepsilon_0 t) \\ K^+(\lambda) &= \int_0^\infty dt e^{-\lambda t} h^+(t) \cos(\varepsilon_0 t) \\ K^-(\lambda) &= \int_0^\infty dt e^{-\lambda t} h^-(t) \sin(\varepsilon_0 t). \end{aligned} \quad (17)$$

Here  $K^\pm(\lambda) = \int_0^\infty d\tau e^{-\lambda\tau} \mathcal{K}^\pm(\tau)$  is the Laplace transform of the pump-averaged kernels in Eq. (23) with  $\varepsilon_p = 0$ . The kernels  $K^\pm(\lambda)$  are related to the forward and backward rates  $K^{f/b}(\lambda)$ , introduced in Eq. (6), by  $K^\pm = K^f \pm K^b$ . For devices I and II, in the

absence of pump driving, we analytically evaluated the integrals in Eq. (17) and used the resulting expressions in the susceptibility  $\chi$ , Eq. (16), to perform fits to the data. In the limit  $\omega_p \tau_{\text{env}} \ll 1$ , Eq. (16) simplifies to Eq. (8) of the main text.

#### IV. Coherent-to-incoherent transition

In the absence of probe driving,  $\varepsilon_p = 0$ , the population difference  $P(t)$  is conveniently obtained by introducing the Laplace transform  $\hat{P}(\lambda) = \int_0^\infty dt e^{-\lambda t} P(t)$ . From Eq. (10) one finds

$$\hat{P}(\lambda) = \frac{1 - K^-(\lambda)/\lambda}{\lambda + K^+(\lambda)}. \quad (18)$$

The pole in  $\lambda = 0$  determines the asymptotic value  $P_0 = K^-(0)/K^+(0)$  reached at long times. The solution of the equation  $\lambda + K^+(\lambda) = 0$  yields information on the transient dynamics. In the underdamped regime, complex solutions yield the renormalized tunneling frequency with associated dephasing rate. In the incoherent regime, the long-time dynamics is ruled by a single exponential decay with relaxation rate  $\gamma_d \equiv K^+(\lambda = 0)$  cf. Eq. (17).

Let us focus exemplarily on the undriven spin-boson system at the symmetry point  $\varepsilon_0 = 0$ . Then, an expansion around  $\lambda = 0$  yields a quadratic equation for the poles of  $\hat{P}(\lambda)$  [30]. In the coherent regime the roots are complex conjugated,  $\lambda_{1,2} = -\gamma \pm i\Omega(T)$ , while they are real in the incoherent regime (cf. inset in Figs. 2 (a-c)). The temperature  $T^*$  at which the oscillation frequency  $\Omega(T)$  vanishes determines the transition between the coherent and incoherent regimes. For weak coupling one finds for example  $\Omega = \Delta_r(1 - \pi\alpha\hbar\Delta_r/k_B T)$  with

$$\Delta_r = \Delta(\Delta/\omega_c)^{\alpha/(1-\alpha)} g(\alpha) \quad (19)$$

and  $g(\alpha) = [\Gamma(1 - 2\alpha) \cos(\pi\alpha)]^{1/2(1-\alpha)}$ . This allows the estimate  $T^*(\alpha) \approx \frac{\hbar\Delta_r}{k_B\alpha}$  when  $\alpha \ll 1$ . For general  $\alpha < 1$  it is given by

$$T^*(\alpha) \approx \frac{\hbar\Delta_r}{k_B} [\Gamma(\alpha)/\alpha\Gamma(1 - \alpha)]^{1/2(1-\alpha)}, \quad (20)$$

where  $\Gamma(x)$  is the Euler Gamma function. This approximate expression matches well the numerically calculated crossover temperature shown in Fig. 1(c). The coherent-incoherent

transition temperature  $T^*(\alpha)$  depicted there is established, for  $\alpha < 0.5$ , by using Eq. (16), with numerically evaluated kernels, whereas the point at  $\alpha = 0.5$  is individuated by the exact result  $k_B T^*(\alpha = 0.5)/\hbar\Delta = \Delta/2\omega_c$  [1]. Further details are found in the Supplement.

## Acknowledgments

The authors acknowledge financial support by the Deutsche Forschungsgemeinschaft via SFB 631, NSERC of Canada, the Canadian Foundation for Innovation, the Ontario Ministry of Research and Innovation, Industry Canada and Canadian Microelectronics Corporation. L.M. gratefully acknowledges financial support by Angelo Della Riccia Foundation and hospitality by Regensburg University during the early stages of the project. The authors thank J. J. García-Ripoll, P. Hänggi, and B. Peropadre for fruitful discussions and S. Chang, A. M. Vadiraj and C. Deng for help with device fabrication and with the measurement setups.

## Author contributions

L.M. and M.G. performed the theoretical analysis, with numerical simulations carried out by L.M. The experiments were designed and performed by P. F.-D., A. L., and C.W.. The devices were fabricated by P.F.-D., J.-L.O., M.A.Y. and M.R.O. contributed to device design and fabrication. R.B. assisted in numerical modeling of the device. The manuscript was mainly written by M. G. with critical comments provided by all authors. The Supplementary Material was mainly written by L.M..

---

[1] Leggett, A. J. *et al.* Dynamics of the dissipative two-state system. *Rev. Mod. Phys.* **59**, 1-85 (1987).

- [2] Weiss, U. *Quantum dissipative systems* (World Scientific Singapore, fourth ed. 2012).
- [3] Golding, B., Zimmerman, M. N., and Coppersmith, S. N. Dissipative Quantum Tunneling of a Single Microscopic Defect in a Mesoscopic Metal. *Phys. Rev. Lett.* **68**, 998 (1992).
- [4] Golding, B., Graebner, J. E., Kane, A. B., Black, J. L. Relaxation of tunneling systems by conduction electrons in a metallic glass. *Phys. Rev. Lett.* **41**, 1487 (1978).
- [5] Han, S., Lapointe J., Lukens, J. E. Observation of incoherent relaxation by tunneling in a macroscopic two-state system. *Phys. Rev. Lett.* **66**, 810 (1991).
- [6] Morillo, M., Cukier R. I. Solvent effects on proton transfer reactions *J. Chem. Phys.* **91**, 857 (1989).
- [7] Forn-Díaz, P. *et al.* Ultrastrong coupling of an artificial atom to an electromagnetic continuum. *Nature Phys.* **13**, 39-43 (2017).
- [8] Peropadre, B., Zueco, D., Porras, D., García-Ripoll, J. J. Nonequilibrium and nonperturbative dynamics of ultrastrong coupling in open lines. *Phys. Rev. Lett.* **111**, 243602 (2013).
- [9] Yoshihara, F. *et al.* Superconducting qubit-oscillator circuit beyond the ultrastrong-coupling regime. *Nature Phys.* **13**, 44-47 (2017).
- [10] Grifoni, M. and Hänggi P. Driven quantum tunneling. *Phys. Rep.* **304**, 229-358 (1998).
- [11] Nakamura, Y., Pashkin, Yu. A., and Tsai, J. S., Rabi oscillations in a Josephson-Junction Charge Two-Level System. *Phys. Rev. Lett.* **87**, 246601 (2001).
- [12] Wilson, C. M. *et al.* Coherence Times of Dressed States of a Superconducting Qubit under Extreme Driving. *Phys. Rev. Lett.* **98**, 257003 (2007).
- [13] Wilson, C. M. *et al.* Dressed relaxation and dephasing in a strongly driven two-level system. *Phys. Rev. B* **81**, 024520 (2010).
- [14] Oliver, W. D., *et al.* Mach-Zehnder Interferometry in a Strongly Driven Superconducting Qubit. *Science* **310**, 1653-1657 (2005).
- [15] Sillanpää, M., Lehtinen, T., Paila, A., Makhlin, Y., and Hakonen, P. Continuous-time monitoring of Landau-Zener interference in a Cooper pair box. *Phys. Rev. Lett.* **96**, 187002 (2006).

- [16] Berns, D. *et al.* Amplitude spectroscopy of a solid-state artificial atom. *Nature* **455**, 51-57 (2008).
- [17] Deng, C. *et al.* Observation of Floquet states in a strongly driven artificial atom. *Phys. Rev. Lett.* **115**, 133601 (2015).
- [18] Mooij, J. E. *et al.* Josephson persistent-current qubit. *Science* **285**, 1036-1039 (1999).
- [19] Grifoni, M., Sassetti, M. Hänggi., P., and Weiss., U. Cooperative effects in the nonlinearly driven spin-boson system. *Phys. Rev. E* **52**, 3596 (1995).
- [20] Kubo, R. Statistical Mechanics of irreversible processes. *J. Phys. Soc. Jap.* **12**, 570-586 (1957).
- [21] Temperature, cutoff frequency, renormalized splitting  $\Omega$ , and conversion factor  $\mathcal{N}$  are estimated from the experiments. Some deviations in the choice of these parameters can yield a small variation in the estimate of the coupling strength  $\alpha$ .
- [22] Díaz-Camacho, G., Bermudez, A., García-Ripoll, J. J. Dynamical polaron ansatz: a theoretical tool for the ultra-strong coupling regime of circuit QED. *Phys. Rev. A* **93**, 043843 (2016).
- [23] Shi, T., Chang, Y., García-Ripoll, J. J. Ultrastrong coupling few-photon scattering theory. arxiv:1701.04709 (2017).
- [24] Shevchenko, S. N., Ashhab, S., and Nori., F. Landau-Zener-Stückelberg interferometry. *Phys. Rep.* **492**, 1-30 (2010).
- [25] Hausinger, J., and Grifoni, M. Dissipative two-level system under strong ac-driving: a combination of Floquet and Van Vleck perturbation theory. *Phys. Rev. A* **81**, 022117 , (2010).
- [26] Grossmann, F., Dittrich, T., Jung, P., and Hänggi, P. Coherent destruction of tunneling. *Phys. Rev. Lett.* **67**, 516-519 (1991).
- [27] Dakhnovski, Y., and Coalson, R. D. Manipulating reactant-product distributions in electron transfer reactions with a laser field. *J. Chem. Phys.* **103** 2908-2916 (1995).
- [28] Goychuk, I. A., Petrov, E. G., and May, V. Control of the dynamics of a dissipative two-level system by a strong periodic field. *Chem. Phys. Lett.* **253**, 428 - 437 (1996).

- [29] Caldeira, O., and Leggett, A. J. Quantum tunneling in a dissipative system. *Ann. Phys.* **149**, 374-456 (1987).
- [30] Weiss, U. and Grabert, H. Effects of temperature and bias on macroscopic quantum coherence. *Europhys. Lett.* **2**, 667 (1986).

# Supplementary Information

## I. EVALUATION OF THE TRANSMISSION WITHIN NIBA

### A. Generalized master equation

The spin-boson model describes a two-level system – the qubit – interacting with an environment of quantum harmonic oscillators, the so-called heat bath.

The total Hamiltonian of the model reads

$$H(t) = -\frac{\hbar}{2} [\Delta\sigma_x + \varepsilon(t)\sigma_z] - \frac{\hbar}{2}\sigma_z \sum_i c_i (a_i^\dagger + a_i) + \sum_i \hbar\omega_i a_i^\dagger a_i, \quad (21)$$

where  $\sigma_j$  are Pauli spin operators and  $a_i^\dagger$  and  $a_i$  are bosonic creation and annihilation operators, respectively. Within the noninteracting-blip approximation (NIBA), the time evolution of the qubit's population difference  $P(t) = \langle \sigma_z(t) \rangle$  is governed by the following generalized master equation (GME) [1–3]

$$\dot{P}(t) = \int_{t_0}^t dt' [\mathcal{K}^-(t, t') - \mathcal{K}^+(t, t')P(t')] . \quad (22)$$

In the presence of a time dependent bias described by  $\varepsilon(t) = \varepsilon_0 + \varepsilon_p \cos(\omega_p t) + \varepsilon_d \cos(\omega_d t)$ , where the subscript "p" and "d" denote *probe* and *drive*, respectively, the exact NIBA kernels read

$$\begin{aligned} \mathcal{K}_N^+(t, t') &= \Delta^2 e^{-Q'(t-t')} \cos[Q''(t-t')] \cos[\zeta_{\text{tot}}(t, t')] , \\ \mathcal{K}_N^-(t, t') &= \Delta^2 e^{-Q'(t-t')} \sin[Q''(t-t')] \sin[\zeta_{\text{tot}}(t, t')] , \end{aligned} \quad (23)$$

where the total dynamical phase has the form

$$\zeta_{\text{tot}}(t, t') = \int_{t'}^t dt'' \varepsilon(t'') . \quad (24)$$

Averaging over a period  $2\pi/\omega_d$  yields an effective description of the drive by means of the following NIBA kernels [3], which we use for our calculations

$$\begin{aligned} \mathcal{K}^+(t, t') &= h^+(t-t') \cos[\zeta(t, t')] , \\ \mathcal{K}^-(t, t') &= h^-(t-t') \sin[\zeta(t, t')] . \end{aligned} \quad (25)$$

The functions  $h^\pm(t)$  in Eq. (25) read

$$\begin{aligned} h^+(t) &= \Delta^2 e^{-Q'(t)} \cos[Q''(t)] J_0 \left[ \frac{2\varepsilon_d}{\omega_d} \sin\left(\frac{\omega_d t}{2}\right) \right], \\ h^-(t) &= \Delta^2 e^{-Q'(t)} \sin[Q''(t)] J_0 \left[ \frac{2\varepsilon_d}{\omega_d} \sin\left(\frac{\omega_d t}{2}\right) \right]. \end{aligned} \quad (26)$$

The dynamical phase

$$\zeta(t, t') = \varepsilon_0(t - t') + \frac{\varepsilon_p}{\omega_p} [\sin(\omega_p t) - \sin(\omega_p t')] \quad (27)$$

entering the averaged NIBA kernels in Eq. (25) accounts now exclusively for the static bias and the probe field, whereas the drive is taken into account, in an effective description, by the Bessel functions  $J_0$  in the functions of  $h^\pm(t)$ , see Eq. (26).

The functions  $Q'$  and  $Q''$  in Eqs. (23) and (26), are the real and imaginary part of the bath correlation function  $Q(t)$ , respectively. For Ohmic spectral density function  $G(\omega) = 2\alpha\omega \exp(-\omega/\omega_c)$ ,  $\alpha$  being the dimensionless coupling strength and  $\omega_c$  a high frequency cutoff, these two functions read explicitly [1]

$$\begin{aligned} Q'(t) &= \alpha \ln(1 + \omega_c^2 t^2) + 4\alpha \ln \left| \frac{\Gamma(1 + \omega_\beta/\omega_c)}{\Gamma(1 + \omega_\beta/\omega_c + i\omega_\beta t)} \right|, \\ Q''(t) &= 2\alpha \arctan(\omega_c t), \end{aligned} \quad (28)$$

where we have introduced the thermal frequency  $\omega_\beta = (\hbar\beta)^{-1}$  and where  $\Gamma(x)$  is the Euler Gamma function. In the limit  $\hbar\omega_c \gg k_B T$  (or  $\omega_c \gg \omega_\beta$ ), neglecting the ratio  $\omega_\beta/\omega_c$  and using  $\Gamma(1 + ix)\Gamma(1 - ix) = \pi x / \sinh(\pi x)$ , we get the so-called *scaling limit* forms

$$\begin{aligned} Q'(t) &= 2\alpha \ln \left[ \sqrt{1 + \omega_c^2 t^2} \frac{\sinh(\pi\omega_\beta t)}{\pi\omega_\beta t} \right], \\ Q''(t) &= 2\alpha \arctan(\omega_c t). \end{aligned} \quad (29)$$

The above formulas are accurate in every regime, provided that the cutoff frequency is large with respect to the other frequency scales involved. For  $\omega_c t \gg 1$ , these functions assume the approximated form

$$\begin{aligned} Q'(t) &\simeq 2\alpha \ln \left[ \frac{\omega_c}{\pi\omega_\beta} \sinh(\pi\omega_\beta t) \right], \\ Q''(t) &\simeq \pi\alpha \operatorname{sgn}(t). \end{aligned} \quad (30)$$

Especially at high temperature,  $\omega_\beta \sim \Delta$ , the cutoff operated by the real part  $Q'(t)$  in the kernels (25), becomes of purely exponential form on a short time scale, see Eq. (31) below. Now, this means that, at strong coupling, the kernels go to zero on a rather short time, where the short time behavior of  $Q''$ , neglected in Eq. (30), is relevant. Therefore we will use the approximated expressions (30) only for  $\alpha < 0.5$ .

An insight into the different behaviors shown by the two driven setups in Fig. 3 of the main text, is provided by considering the memory time of the kernels (25). To this end, consider the long-time limit of  $Q(t)$  in Eq. (30). Specifically, for  $\omega_\beta t = tk_B T/\hbar \gg 1$ , the real part of  $Q(t)$  assumes the form

$$Q'(t) \sim t/\tau_{\text{env}} + \text{const.}, \quad \text{where} \quad \tau_{\text{env}} = (2\pi\alpha k_B T/\hbar)^{-1}. \quad (31)$$

This form implies that, at fixed, finite temperature,  $\tau_{\text{env}}$  decreases as the coupling  $\alpha$  is increased. Moreover, in the above limit, the bath force operator  $F(t)$  of the quantum Langevin equation for the spin-boson model is delta-correlated, as  $\langle F(t)F(0) \rangle \propto \frac{d^2}{dt^2} Q(|t|)$ , where the average is taken with respect to the thermal state of the bath (see Ref. [1] for details). As a consequence, on the time scale dictated by the limit (31) the bath is a white noise source.

## B. Relation between transmission and qubit dynamics

Consider the situation depicted in Fig 4, in which the probe voltage field  $V_p^{\text{in}}(t) = f_Z \varepsilon_p \cos(\omega_p t)$ , coming from the left, is scattered by the qubit placed at the center of the transmission line. The proportionality constant  $f_Z$  has dimensions of flux whereas  $\varepsilon_p$  is an angular frequency. The scattering at the qubit position results in the transmitted field to the right,  $V_{\text{transm}}(t)$ , and a reflected field to the left,  $V_{\text{refl}}(t)$ . The flux difference across the qubit is  $\delta\Phi(t) = \Phi^L(t) - \Phi^R(t)$ , the flux being related to the voltage by  $\Phi(t) = \int_{-\infty}^t dt' V(t')$ .

A discretized circuit model [4] with inductance and capacitance per unit length  $l$  and  $c$ , respectively, gives for the voltage  $V(0^-, t) \equiv V^L(t)$  and current  $I(0^-, t) \equiv I^L(t)$

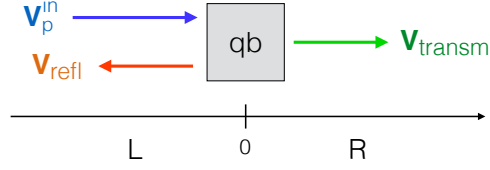


FIG. 4. Reflection and transmission of the incoming voltage  $V_p^{\text{in}}$ .

immediately to the left of the qubit the following equations

$$\begin{aligned} V^L(t) &= V_p^{\text{in}}(t) + V_{\text{refl}}(t) , \\ I^L(t) &= \frac{1}{Z} [V_p^{\text{in}}(t) - V_{\text{refl}}(t)] , \end{aligned} \quad (32)$$

where  $Z = \sqrt{l/c}$  is the characteristic impedance of the transmission line. Similarly, to the right of the qubit, where we set  $V(0^+, t) \equiv V^R(t)$  and  $I(0^+, t) \equiv I^R(t)$ , we have

$$\begin{aligned} V^R(t) &= V_{\text{transm}}(t) , \\ I^R(t) &= \frac{1}{Z} V_{\text{transm}}(t) . \end{aligned} \quad (33)$$

Using the conservation of the current,  $I^L(t) = I^R(t)$ , and the relation  $V^L(t) - V^R(t) = \delta\dot{\Phi}(t)$ , from Eqs. (32) and (33) we get

$$V_{\text{transm}}(t) = V_p^{\text{in}}(t) - \frac{\delta\dot{\Phi}(t)}{2} . \quad (34)$$

We identify the flux difference across the qubit with the population difference of the localized eigenstates of the flux operator  $\hat{\Phi} = f\sigma_z$ , namely we set  $\delta\Phi(t) \equiv f\langle\sigma_z(t)\rangle = fP(t)$ , where  $f$  is the proportionality constant with dimensions of flux, as described in the main text.

Let  $P^{\text{st}}(t) = \lim_{t \rightarrow \infty} P(t)$  be the stationary nonequilibrium population difference, i.e. the asymptotic form of  $P(t)$ . For periodic driving with period  $2\pi/\omega_p$ , the time derivative  $\dot{P}^{\text{st}}(t)$  can be expanded as the Fourier series

$$\dot{P}^{\text{st}}(t) = \sum_m im\omega_p p_m e^{im\omega_p t} , \quad (35)$$

where

$$p_m = \frac{\omega_p}{2\pi} \int_{-\pi/\omega_p}^{\pi/\omega_p} dt P^{\text{st}}(t) e^{-im\omega_p t} . \quad (36)$$

The transmission  $\mathcal{T}$  at frequency  $\omega_p$  ( $m = 1$ ) is defined as the following ratio between transmitted and input voltages

$$\begin{aligned} \mathcal{T}(\omega_p) &= \frac{V_{\text{transm}}(\omega_p)}{V_{\text{p}}^{\text{in}}(\omega_p)} \\ &= \frac{f_Z \varepsilon_p / 2 - i f \omega_p p_1 / 2}{f_Z \varepsilon_p / 2} \\ &= 1 - i \mathcal{N} \omega_p p_1 / \varepsilon_p , \end{aligned} \quad (37)$$

where  $\mathcal{N} = f/f_Z$  and where, in passing from the first to the second line, we used Eqs. (34) and (35). Real and imaginary parts of the transmission are therefore given by

$$\begin{aligned} \text{Re}\{\mathcal{T}(\omega_p)\} &= 1 + \mathcal{N} \omega_p \text{Im}\{p_1\} / \varepsilon_p \\ \text{and} \quad \text{Im}\{\mathcal{T}(\omega_p)\} &= -\mathcal{N} \omega_p \text{Re}\{p_1\} / \varepsilon_p , \end{aligned} \quad (38)$$

respectively.

## II. LINEAR RESPONSE (WEAK PROBE)

### A. Asymptotic population difference in linear response

In the regime of linear response to an applied monochromatic probe driving, namely for small ratio  $\varepsilon_p/\omega_p$ , and within the effective description of the pump drive introduced in Sec. I A, the asymptotic population difference  $P^{\text{st}}(t)$  is monochromatic [3, 5]. It can be thus expressed as the truncated Fourier sum

$$\begin{aligned} P^{\text{st}}(t) &\simeq p_0 + p_1^{(1)} e^{i\omega_p t} + p_{-1}^{(1)} e^{-i\omega_p t} \\ &= P_0 + \hbar \varepsilon_{\text{pr}} [\chi(\omega_p) e^{i\omega_p t} + \chi(-\omega_p) e^{-i\omega_p t}] , \end{aligned} \quad (39)$$

where the superscript <sup>(1)</sup> denotes first order with respect to the ratio  $\varepsilon_p/\omega_p$ . Here  $\chi$  is the linear susceptibility [5] and  $P_0$  is the asymptotic value of  $P(t)$  in absence of probe

driving. As shown in Fig 5 below, this constitutes an excellent approximation of the actual dynamics under weak probe driving. From Eqs. (37) and (39), the transmission at probe frequency in linear response is related to the dynamical susceptibility by

$$\mathcal{T}(\omega_p) = 1 - i\mathcal{N}\hbar\omega_p\chi(\omega_p). \quad (40)$$

Within the NIBA, by substituting the expression (39) for  $P^{\text{st}}(t)$  in the GME (22), setting the upper integration limit to  $t \rightarrow \infty$ , which is valid for times much larger than the kernels' memory time, and expanding the kernels in Fourier series, we get the following closed, linear response expression for  $p_1^{(1)}$  [3, 5]

$$p_1^{(1)}(\omega_p) = \frac{1}{i\omega_p + v^{+(0)}(\omega_p)} \left[ k_1^{-(1)}(\omega_p) - k_1^{+(1)}(\omega_p) \frac{k_0^{-(0)}}{k_0^{+(0)}} \right] \quad (41)$$

(superscripts  $^{(0,1)}$  denote the order in  $\varepsilon_p/\omega_p$ ).

The kernels  $k_m^\pm$  and  $v^+$ , whose approximate forms (perturbative in  $\varepsilon_p/\omega_p$ ) enter Eq. (41), are defined by

$$\begin{aligned} k_m^\pm(\omega_p) &= \frac{\omega_p}{2\pi} \int_{-\pi/\omega_p}^{\pi/\omega_p} dt e^{-im\omega_p t} \int_0^\infty d\tau \mathcal{K}^\pm(t, t - \tau), \\ v^+(\omega_p) &= \frac{\omega_p}{2\pi} \int_{-\pi/\omega_p}^{\pi/\omega_p} dt \int_0^\infty d\tau e^{-i\omega_p \tau} \mathcal{K}^\pm(t, t - \tau), \end{aligned} \quad (42)$$

where the pump drive-averaged kernels  $\mathcal{K}^\pm(t, t')$  have been introduced in Eq. (25). Expansion of the Bessel functions entering the kernels  $\mathcal{K}^\pm(t, t')$  to lowest order in  $\varepsilon_p/\omega_p$  by means of  $J_n(x) \sim (x/2)^n$ , yields the following explicit expressions for the kernels in

Eq. (41)

$$\begin{aligned}
k_0^{+(0)} &= \int_0^\infty dt h^+(t) \cos(\varepsilon_0 t) , \\
k_0^{-(0)} &= \int_0^\infty dt h^-(t) \sin(\varepsilon_0 t) , \\
k_1^{+(1)}(\omega_p) &= -\frac{\varepsilon_p}{\omega_p} \int_0^\infty dt e^{-i\omega_p t/2} h^+(t) \sin(\varepsilon_0 t) \sin(\omega_p t/2) , \\
k_1^{-(1)}(\omega_p) &= \frac{\varepsilon_p}{\omega_p} \int_0^\infty dt e^{-i\omega_p t/2} h^-(t) \cos(\varepsilon_0 t) \sin(\omega_p t/2) , \\
\text{and } v^{+(0)}(\omega_p) &= \int_0^\infty dt e^{-i\omega_p t} h^+(t) \cos(\varepsilon_0 t) , \tag{43}
\end{aligned}$$

with  $h^\pm(t)$  defined in Eq. (26). In Fig. 5 the transient dynamics obtained from direct integration of the GME (22) is compared to the asymptotic time-periodic evolution given by Eqs. (39), (41), and (43).

### B. Evaluation of the linear susceptibility $\chi$

The linear susceptibility  $\chi$  is related to the coefficient  $p_1^{(1)}$  by Eq. (39). Thus, from Eq. (41), by simplifying the notation, we get

$$\chi(\omega_p) = \frac{H^+(\omega_p) - H^-(\omega_p)P_0}{i\omega_p + K^+(i\omega_p)} , \quad \text{where} \quad P_0 = K^-(0)/K^+(0) . \tag{44}$$

Here  $K^\pm(\lambda) = \int_0^\infty d\tau e^{-\lambda\tau} \mathcal{K}^\pm(\tau)$  is the Laplace transform of the pump-averaged kernels with  $\varepsilon_p = 0$ . The kernels in Eq. (26) are related to those defined in Eq. (43) by the relations

$$K^\pm(\lambda = 0) = k_0^{\pm(0)} , \quad K^+(\lambda = i\omega_p) = v^{+(0)}(\omega_p) , \quad \text{and} \quad H^\pm(\omega_p) = \frac{k_1^{\mp(1)}(\omega_p)}{\hbar\varepsilon_p} . \tag{45}$$

Note that, within the present linear response treatment, the transmission is independent of the probe amplitude  $\varepsilon_p$ , cf. Eq. (40). Note also that notation for the kernels  $H^\pm$  reflects

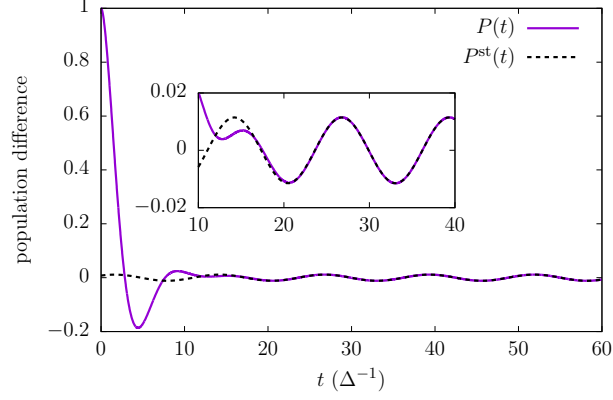


FIG. 5. Linear response to probe – dynamics of the undriven qubit. Time evolution of the population difference  $P(t)$  obtained by integrating the GME (22) with  $P(0) = 1$  (solid line) compared with the asymptotic dynamics  $P^{\text{st}}(t)$  given by Eq. (39) with  $p_1^{(1)}$  from Eq. (41) (dashed line). The kernels  $k_m^\pm$  and  $v^+$  are obtained by numerically evaluating the integrals (43). The bath correlation function  $Q(t)$  in exact scaling limit form (Eq. (29)) is used for both curves. Parameters are  $\alpha = 0.2$ ,  $T = 0.5 \hbar\Delta/k_B$ ,  $\omega_c = 10 \Delta$ ,  $\varepsilon_0 = 0$ ,  $\varepsilon_d = 0$ ,  $\omega_p = 0.5 \Delta$ , and  $\varepsilon_p = 0.01 \Delta$ .

the same symmetry with respect to the static bias  $\varepsilon_0$  which holds for  $K^\pm$ . Finally the forward/backward rates

$$K^{f/b} = \frac{\Delta^2}{2} \int_0^\infty dt e^{-Q'(t)} J_0 \left[ \frac{2\varepsilon_d}{\omega_d} \sin \left( \frac{\omega_d t}{2} \right) \right] \cos[Q''(t) \mp \varepsilon_0 t], \quad (46)$$

introduced in the main text are related to the rates  $K^\pm(0)$  defined in Eq. (45) by

$$K^{f/b} = \frac{K^+(0) \pm K^-(0)}{2}. \quad (47)$$

1. *Approximate form of  $\chi$*

Whenever the condition  $\omega_p \tau_{\text{env}} \ll 1$  is fulfilled, it is possible to expand the kernels  $K^+(i\omega_p)$  and  $H^\pm(\omega_p)$  (see Eq. (45)) with respect to  $\omega_p \tau_{\text{env}}$ . To first order

$$\begin{aligned} K^+(i\omega_p) &\simeq K^+(\lambda = 0) \\ H^\pm(\omega_p) &\simeq \frac{1}{2\hbar} \frac{\partial}{\partial \varepsilon_0} K^\mp(\lambda = 0) . \end{aligned} \quad (48)$$

Now, the NIBA prediction for the stationary probability difference  $P_0$  in the absence of the pump driving is  $P_0 = \tanh(\hbar\varepsilon_0/2k_B T)$  [1, 3]. In the presence of the pump driving, within the present effective description of the pump drive (see Sec. I A), the expression for  $P_0$  is generalized as follows

$$P_0 = \tanh\left(\frac{\hbar\varepsilon_{\text{eff}}}{2k_B T}\right) \quad \text{where} \quad \varepsilon_{\text{eff}} = \frac{k_B T}{\hbar} \ln\left(\frac{K^f}{K^b}\right) . \quad (49)$$

The effective bias  $\varepsilon_{\text{eff}}$  depends on the static bias  $\varepsilon_0$ . As a result, in the limit  $\omega_p \tau_{\text{env}} \ll 1$ , by substituting the expressions (48) into Eq. (44) we get

$$\begin{aligned} \chi(\omega_p) &\simeq \frac{K^+(0)}{2\hbar[i\omega_p + K^+(0)]} \frac{\partial}{\partial \varepsilon_0} \tanh\left(\frac{\hbar\varepsilon_{\text{eff}}}{2k_B T}\right) \\ &= \frac{1}{4k_B T} \frac{\partial \varepsilon_{\text{eff}} / \partial \varepsilon_0}{\cosh^2(\hbar\varepsilon_{\text{eff}}/2k_B T)} \frac{\gamma_d}{\gamma_d + i\omega_p} , \end{aligned} \quad (50)$$

where  $\gamma_d = K^+(0) = K^f + K^b$  (cf. Eq. 47), and where

$$\frac{\partial \varepsilon_{\text{eff}}}{\partial \varepsilon_0} = \frac{k_B T}{\hbar} \left( \frac{1}{K^f} \frac{\partial K^f}{\partial \varepsilon_0} - \frac{1}{K^b} \frac{\partial K^b}{\partial \varepsilon_0} \right) . \quad (51)$$

At the symmetry point  $\varepsilon_{\text{eff}} = \varepsilon_0 = 0$  and from Eqs. (46) and (51) we get

$$\lim_{\varepsilon_0 \rightarrow 0} \frac{\partial \varepsilon_{\text{eff}}}{\partial \varepsilon_0} = \frac{2k_B T}{\hbar} \frac{\int_0^\infty dt t h^-(t)}{\int_0^\infty dt h^+(t)} , \quad (52)$$

where the functions  $h^\pm(t)$  have been defined in Eq. (26).

### C. Analytical evaluation of the kernels in the absence of pump driving, $\varepsilon_d = 0$

The integrals in Eq. (43) can be solved analytically by using the bath correlation function  $Q(t)$  in the approximated scaling limit form (30) for  $\alpha < 1/2$ . With this approximated correlation function, the functions  $h^\pm(t)$ , introduced in Eq. (26), take on the form

$$\begin{aligned} h^+(t) &= \Delta^2 (2\kappa\omega_c)^{-2\alpha} [\sinh(t/2\kappa)]^{-2\alpha} \cos(\pi\alpha), \\ h^-(t) &= \Delta^2 (2\kappa\omega_c)^{-2\alpha} [\sinh(t/2\kappa)]^{-2\alpha} \sin(\pi\alpha), \end{aligned} \quad (53)$$

where we introduced the time scale  $\kappa = \hbar\beta/2\pi = (2\pi\omega_\beta)^{-1}$ .

We use the exact result [6]

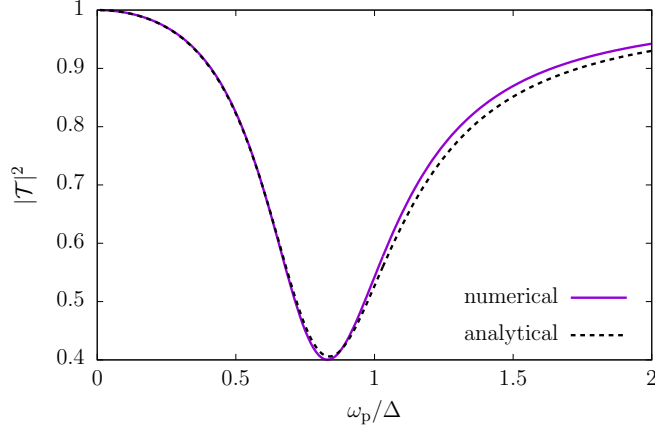


FIG. 6. Transmission vs. probe frequency for the undriven qubit. The transmission is calculated via Eqs. (40) and (44). Solid line – kernels numerically evaluated from Eq. (43) with the bath correlation function  $Q(t)$  in the exact scaling limit from (29). Dashed line – kernels in analytical approximated forms (54). Parameters are  $\alpha = 0.15$ ,  $T = 0.5 \hbar\Delta/k_B$ ,  $\omega_c = 10 \Delta$ ,  $\varepsilon_0 = 0$ ,  $\varepsilon_d = 0$ , and  $\varepsilon_p = 0.01 \Delta$ .

$$\int_0^\infty dt e^{-\mu t} \sinh^\nu(\beta t) = \frac{1}{2^{\nu+1}\beta} B\left(\frac{\mu}{2\beta} - \frac{\nu}{2}, \nu + 1\right),$$

where  $B(x, y)$  is the *beta* function with the property

$$B(x, y) = \frac{\Gamma(x)\Gamma(y)}{\Gamma(x+y)},$$

and  $\Gamma(z)$  is the Euler Gamma function, with the property  $\Gamma(1-z)\Gamma(z) = \pi/\sin(\pi z)$ . By setting  $\mu = i(\omega_p \pm \varepsilon_0)$ ,  $\nu = -2\alpha$ , and  $\beta = (2\kappa)^{-1}$ , we obtain the following analytical expression for the kernels in Eq. (45)

$$\begin{aligned}
K^+(\lambda) &= N_+ [\mathcal{W}(-i\lambda + \varepsilon_0) + \mathcal{W}(-i\lambda - \varepsilon_0)] , \\
K^-(0) &= iN_- [\mathcal{W}(\varepsilon_0) - \mathcal{W}(-\varepsilon_0)] , \\
H^-(\omega_p) &= \frac{1}{2\hbar\omega_p} N_+ [\mathcal{W}(\omega_p + \varepsilon_0) - \mathcal{W}(\omega_p - \varepsilon_0) - \mathcal{W}(\varepsilon_0) + \mathcal{W}(-\varepsilon_0)] , \\
\text{and } H^+(\omega_p) &= i\frac{\varepsilon_p}{2\omega_p} N_- [\mathcal{W}(\omega_p + \varepsilon_0) + \mathcal{W}(\omega_p - \varepsilon_0) - \mathcal{W}(\varepsilon_0) - \mathcal{W}(-\varepsilon_0)] , \quad (54)
\end{aligned}$$

where

$$\begin{aligned}
N_+ &= \frac{\Delta^2 \kappa^{1-2\alpha}}{2 \omega_c^{2\alpha}} \cos(\pi\alpha)\Gamma(1-2\alpha) , \\
N_- &= \frac{\Delta^2 \kappa^{1-2\alpha}}{2 \omega_c^{2\alpha}} \sin(\pi\alpha)\Gamma(1-2\alpha) , \\
\text{and } \mathcal{W}(x) &= \frac{\Gamma(\alpha + i\kappa x)}{\Gamma(1 - \alpha + i\kappa x)} . \quad (55)
\end{aligned}$$

Note that  $\mathcal{W}(-x) = \mathcal{W}^*(x)$ . In Fig. 6, the transmission obtained by using the analytical expressions (54) is compared with the corresponding numerical evaluations from Eq. (43) with  $Q(t)$  in the exact scaling limit form (29).

The analytical expressions (54) are used to perform fits to data (see the next section) and for the theory colormaps in panels (d) and (e) of Fig. 2 ( $\alpha = 0.007$  and  $0.21$ , respectively, and  $\varepsilon_d = 0$ ) of the main text. This is not the case for panel (f) of the same figure ( $\alpha = 0.8$ ,  $\varepsilon_d = 0$ ) and for Fig. 3 ( $\varepsilon_d \neq 0$ ) of the main text, where the transmission is calculated by numerically evaluating the integrals (43) with correlation function  $Q(t)$  in the exact scaling limit form (29).

#### D. Fit to data for devices I and II in the absence of pump driving

In Fig. 7 we show the results of fits to the measured transmission at the symmetry point ( $\Phi_\epsilon = \Phi_0/2$ , where  $\Phi_\epsilon$  is the control field associated with the static bias) for the

devices I and II. The spectra of these devices in the absence of drive are shown in Fig. 2 (d-e) of the main text. Fits to data are performed by using Eqs. (40) and (44) with the analytical expressions (54) for the kernels  $K^\pm$  and  $H^\pm$ . Note that the present treatment has as input the bare value of the qubit splitting  $\Delta$ , which is not accessed directly in experiments. For this reason  $\Delta$  is left as a free parameter, along with the spin-boson coupling  $\alpha$  and the prefactor  $\mathcal{N}$  in Eq. (40). Temperature and cutoff frequency are fixed to  $T = 90$  mK and  $\omega_c/2\pi = 65$  GHz, respectively.

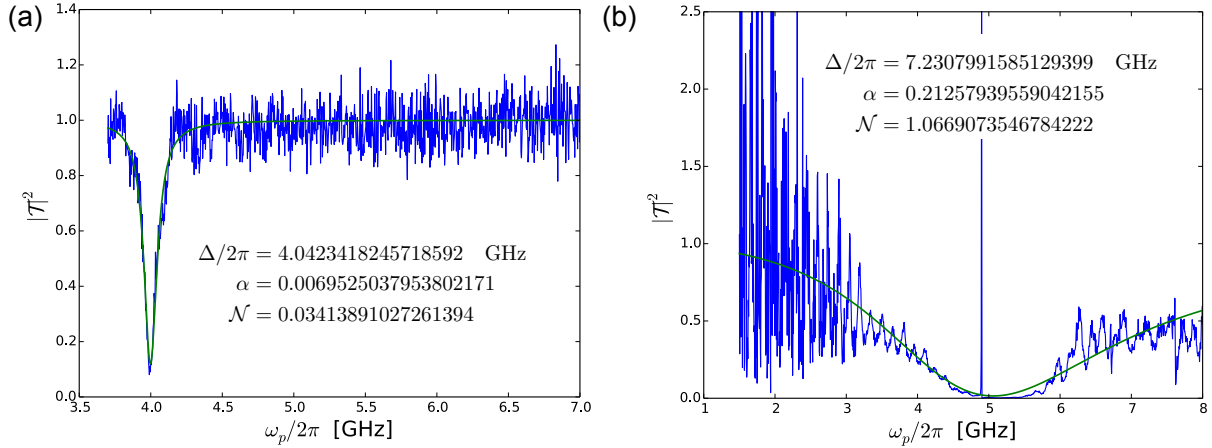


FIG. 7. Transmission  $|\mathcal{T}|^2$  vs probe frequency at the symmetry point ( $\Phi_\epsilon = \Phi_0/2$ ). The results of fit to the transmission data from experiments provide estimates for  $\alpha$ ,  $\Delta$ , and  $\mathcal{N}$ . The analytical expressions (54) are used. **(a)** – Cut at the symmetry point of the spectrum of Device I (see Fig. 2 (d) of the main text). **(b)** – Cut at the symmetry point of the spectrum of Device II (see Fig. 2 (e) of the main text). In both panels, temperature and cutoff frequency are fixed to 90 mK and  $\omega_c/2\pi = 65$  GHz, respectively.

### E. Analytical expression for the qubit's response at weak coupling and zero bias

At weak coupling,  $\alpha \ll 1$ , we can approximate the function  $\mathcal{W}(x)$ , defined in Eq. (55), as follows

$$\begin{aligned} \mathcal{W}(x) &= \frac{1}{\alpha + i\kappa x} \frac{\Gamma(1 + \alpha + i\kappa x)}{\Gamma(1 - \alpha + i\kappa x)}, \\ &\simeq \frac{1}{\alpha + i\kappa x}. \end{aligned} \quad (56)$$

Moreover, at zero static bias,  $\varepsilon_0 = 0$ , both  $H^-$  and  $K^-(0)$  vanish. The resulting expression for the linear susceptibility is

$$\chi(\omega_p) = \frac{H^+(\omega_p)}{i\omega_p + K^+(i\omega_p)}. \quad (57)$$

Using the linear response expression (40), which relates  $\chi(\omega_p)$  to the transmission  $\mathcal{T}(\omega_p)$ , we end up with the following approximated expressions

$$\begin{aligned} \text{Re}\{\mathcal{T}(\omega_p)\} &\simeq 1 - \mathcal{N}N_- \frac{\kappa\omega_p f(\omega_p) + 2N_+(\kappa\omega_p)^2}{(2\alpha N_+)^2 + f^2(\omega_p)}, \\ \text{Im}\{\mathcal{T}(\omega_p)\} &\simeq \mathcal{N} \frac{N_-}{\alpha} \frac{(\kappa\omega_p)^2 f(\omega_p) - 2\alpha^2 N_+ \kappa\omega_p}{(2\alpha N_+)^2 + f^2(\omega_p)}, \end{aligned} \quad (58)$$

where  $f(\omega_p) = \alpha^2\omega_p + \kappa^2\omega_p^3 - 2N_+\kappa\omega_p$ .

From Eq. (57), the imaginary part of the linear susceptibility at zero bias and arbitrary  $\alpha$  reads

$$\chi''(\omega_p) = \frac{\text{Im}\{H^+(\omega_p)\}\text{Re}\{K^+(i\omega_p)\} - \text{Re}\{H^+(\omega_p)\}(\omega_p + \text{Im}\{K^+(i\omega_p)\})}{\text{Re}\{K^+(i\omega_p)\}^2 + (\omega_p + \text{Im}\{K^+(i\omega_p)\})^2}. \quad (59)$$

Now, for  $\alpha \ll 1$ , by using the analytical expressions (54) for  $H^+$  and  $K^+$  with  $\mathcal{W}$  in the approximated form given by Eq. (56), we get

$$\begin{aligned} H^+(\omega_p) &\simeq \frac{\kappa N_- / \hbar}{\alpha^2 + (\kappa\omega_p)^2} \left(1 - i\frac{\kappa}{\alpha}\omega_p\right), \\ K^+(i\omega_p) &\simeq \frac{2\alpha N_+}{\alpha^2 + (\kappa\omega_p)^2} \left(1 - i\frac{\kappa}{\alpha}\omega_p\right), \end{aligned} \quad (60)$$

so that the imaginary part of  $\chi(\omega_p)$  acquires the weak coupling form

$$\chi''(\omega_p) \simeq -\frac{\kappa N_-}{2\hbar\alpha N_+} \frac{\omega_p \text{Re}\{k^+(i\omega_p)\}}{\text{Re}\{K^+(i\omega_p)\}^2 + (\omega_p + \text{Im}\{K^+(i\omega_p)\})^2}. \quad (61)$$

In the regime considered here, the peak described by Eq. (61) is narrow and the function  $\text{Re}\{K^+(i\omega_p)\}$  practically constant within its width (roughly measured by  $\text{Re}\{K^+(i\omega_p)\}$  itself). The position of the peak is thus well approximated by the value  $\omega^*$  obtained upon requiring that  $\omega_p + \text{Im}\{K^+(i\omega_p)\} = 0$ , which yields

$$\omega^* \simeq \frac{\sqrt{2N+\kappa - \alpha^2}}{\kappa}. \quad (62)$$

We remark that this approximate analytical result is valid for the unbiased system,  $\varepsilon_0 = 0$ , in the limit  $\alpha \ll 1$ . We did not make use of the above approximated results in the main text. However, they show how, in the weak coupling regime, the response  $\chi''$  acquires a Lorentzian shape. Deviations from this Lorentzian behavior are found as  $\alpha$  goes beyond the perturbative regime. This can be seen in Fig. 2 (a-c) of the main text and in the next section, where a comparison is made of the qubit response in three different coupling regimes which span the range from weak to ultrastrong coupling.

### III. DYNAMICAL REGIMES FROM TRANSMISSION FOR THE UNDRIVEN SPIN-BOSON

In the linear (weak probe) regime, the intrinsic properties of the qubit are not influenced by the presence of the probe field. The dynamical behavior of the qubit in absence of driving is fully encoded in the imaginary part  $\chi''$  of the linear susceptibility. Specifically, in the underdamped regime, analogously to the damped harmonic oscillator, the position of the peak of  $\chi''$  and its full width at half maximum (FWHM) are related to the renormalized oscillation frequency and to the decay rate of the oscillations, respectively. Thus, according to Eq. (40), by measuring the (real part) of the transmission at weak probe, the imaginary part of the susceptibility  $\chi$  is accessed which contains the information about the dynamical properties of the static qubit.

Consider the case of zero static bias,  $\varepsilon_0 = 0$ . The imaginary part  $\chi''$  of the susceptibility is characterized by a peak centered at a frequency  $\omega^*$  and of FWHM  $2\gamma$ . In the coherent regime, occurring when  $\omega^* > \gamma$ , the dynamics of  $P(t)$  displays damped oscillations with

renormalized oscillation frequency  $\Omega = \sqrt{(\omega^*)^2 - \gamma^2}$  and damping rate  $\gamma$ . The transition to the incoherent regime is determined by the condition  $\omega^* = \gamma$ . The incoherent regime, which is realized for  $\omega^* < \gamma$ , is described by an exponential decay of  $P(t)$  with rate  $\gamma_r$ , the relaxation rate, given in this case by the position of the peak.

As an illustration, let us consider the three different dissipation regimes mentioned

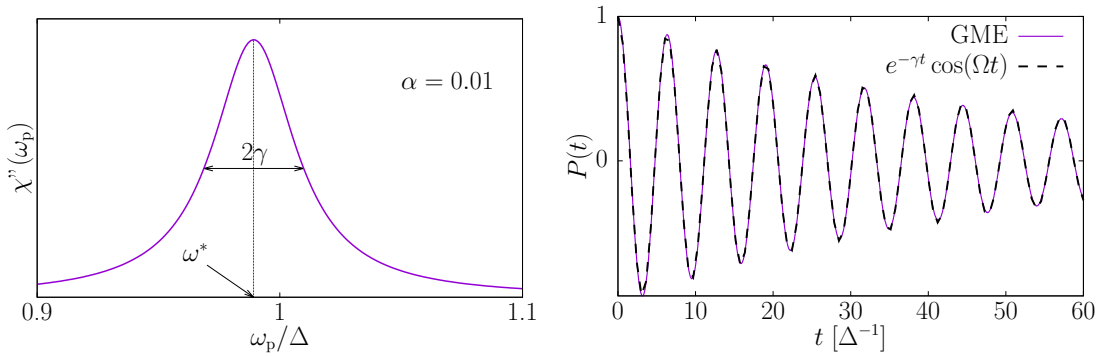


FIG. 8. Dynamical regime from the susceptibility: Coherent regime. *Left panel* – Imaginary part of the linear susceptibility  $\chi(\omega_p)$  (arbitrary units) calculated by means of the analytical expressions in Eq. (54).  $\chi''(\omega_p)$  has a peak at frequency  $\omega^*$  of FWHM  $2\gamma$ . *Right panel* – Comparison between the dynamics obtained from the GME (22), with  $\varepsilon(t) = 0$  and bath correlation function  $Q(t)$  in the exact scaling limit form (29), (solid line) and the damped oscillations with renormalized oscillation frequency and decay rate given by  $\Omega = \sqrt{(\omega^*)^2 - \gamma^2}$  and  $\gamma$ , respectively. Parameters are  $\alpha = 0.01$ ,  $T = 0.5 \hbar\Delta/k_B$ ,  $\varepsilon_0 = 0$ , and  $\omega_c = 10 \Delta$ .

above, namely i) coherent, ii) coherent-incoherent transition, and iii) incoherent. We calculate by Eq. (44) the imaginary part of  $\chi$  as a function of the probe frequency and compare the resulting dynamics, namely damped oscillations or incoherent decay with parameters defined by  $\omega^*$ ,  $\gamma$ , and  $\gamma_r$ , with the dynamics obtained from direct integration of the GME (22) in the static, unbiased case,  $\varepsilon(t) = 0$ . Results are shown in Figs. 8-10.

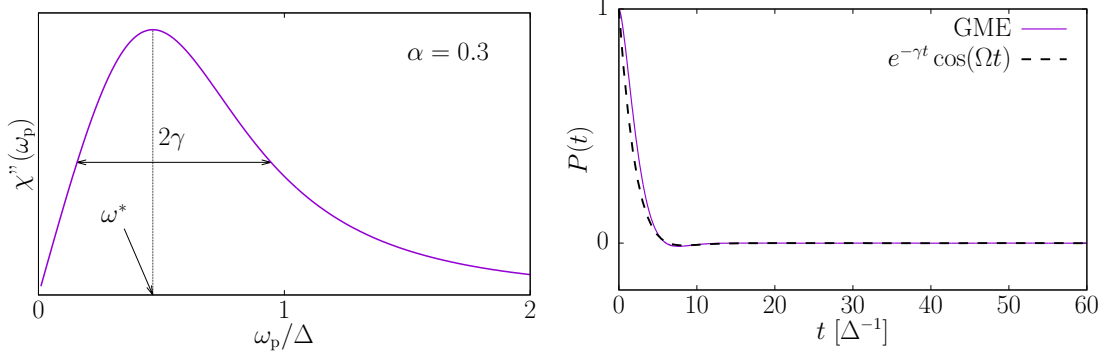


FIG. 9. Dynamical regime from the susceptibility: Coherent-incoherent transition regime. *Left panel* – Imaginary part of linear susceptibility  $\chi(\omega_p)$  (arbitrary units) numerically evaluated by using Eqs. (43)-(45) with bath correlation function  $Q(t)$  in the exact scaling limit form (29).  $\chi''(\omega_p)$  has a peak at frequency  $\omega^*$  of FWHM  $2\gamma$ . *Right panel* – Comparison between the dynamics obtained from the GME (22), with  $\varepsilon(t) = 0$  and bath correlation function  $Q(t)$  from Eq. (29), (solid line) and the damped oscillations with renormalized oscillation frequency and decay rate given by  $\Omega = \sqrt{(\omega^*)^2 - \gamma^2}$  and  $\gamma$ , respectively. Parameters are  $\alpha = 0.3$ ,  $T = 0.5 \hbar\Delta/k_B$ ,  $\varepsilon_0 = 0$ , and  $\omega_c = 10 \Delta$ .

### A. Coherent-to-incoherent transition for the static spin-boson model

On the basis of the considerations made above, we are able to establish a phase diagram for the nondriven spin-boson model, i.e., to assign a dynamical behavior (coherent/incoherent) to the points of the coupling-temperature parameter space, by studying  $\chi''(\omega_p)$ . Specifically, as noted earlier, the condition for the coherent-incoherent transition is  $\omega^* = \gamma$ , where  $\omega^*$  is the position of the peak of  $\chi''(\omega_p)$  and  $2\gamma$  its FWHM.

In Fig. 11 such phase diagram, derived within the NIBA, is shown for  $\omega_c = 10 \Delta$ . The curve, representing the transition temperature  $T^*$  as a function of  $\alpha$ , is an interpolation of the point-set obtained by numerically evaluating  $\chi''(\omega_p)$  by means of Eqs. (43)-(45), with the bath correlation function  $Q(t)$  in exact scaling limit form (29), and searching for the coherent-incoherent transition condition  $\omega^* = \gamma$ . Specifically, fixing the (dimensionless)

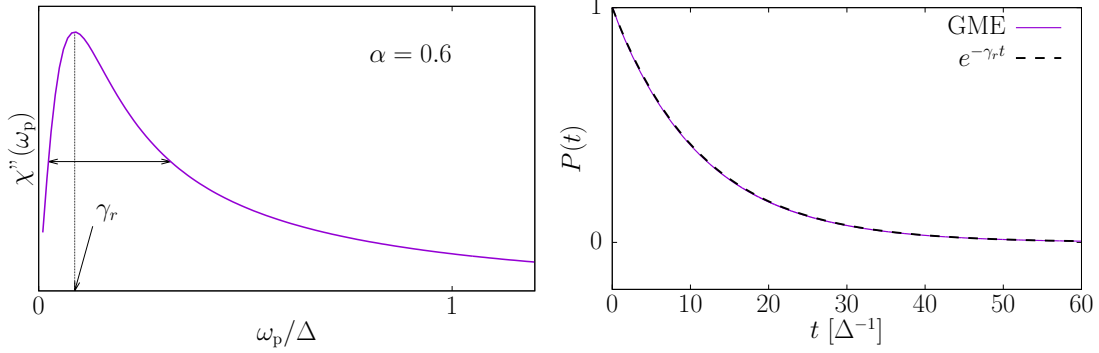


FIG. 10. Dynamical regime from the susceptibility: Incoherent regime. *Left panel* – Imaginary part of the linear susceptibility  $\chi(\omega_p)$  (arbitrary units) numerically evaluated by using Eqs. (43)-(45) with bath correlation function  $Q(t)$  in the exact scaling limit form (29).  $\chi''(\omega_p)$  has a peak at frequency  $\gamma_r$ . *Right panel* – Comparison between the dynamics obtained from the GME (22), with  $\varepsilon(t) = 0$  and bath correlation function  $Q(t)$  from Eq. (29), (solid line) and the exponential decay with rate  $\gamma_r$ . Parameters are  $\alpha = 0.6$ ,  $T = 0.5 \hbar\Delta/k_B$ ,  $\varepsilon_0 = 0$ , and  $\omega_c = 10 \Delta$ .

temperature to the values  $k_B T/\hbar\Delta = 2.5, 2, 1.5, 1, 0.75, 0.5, 0.25$ , and  $0.1$ , a numerical search for the value of  $\alpha$  realizing the condition  $\omega^* = \gamma$  was performed. The lowest point, of abscissa  $\alpha = 0.5$ , is individuated by the exact result  $k_B T^*(\alpha = 0.5)/\hbar\Delta = \Delta/2\omega_c$  [1]. The three full circles in Fig. 11 highlight the parameters used for Figs. 8-10.

- 
- [1] Weiss, U. *Quantum dissipative systems* (World Scientific, Singapore, 4th Ed. 2012).
  - [2] Leggett, A. J. *et al.* Dynamics of the dissipative two-state system. *Rev. Mod. Phys.* **59**, 1-85 (1987).
  - [3] Grifoni, M. and Hänggi P. Driven quantum tunneling. *Phys. Rep.* **304**, 229-358 (1998).
  - [4] Vool, U. and Devoret, M. H. Introduction to quantum electromagnetic circuits. *Int. J. Circ. Theor. Appl.*, doi: 10.1002/cta.2359, (2016).

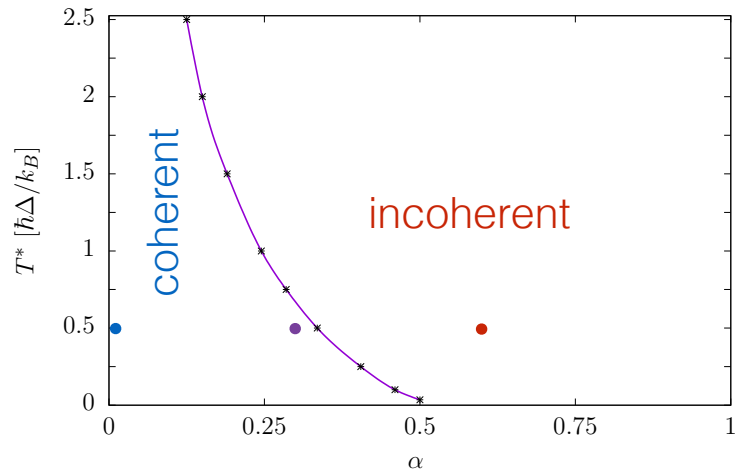


FIG. 11. Coherent-to-incoherent transition temperature  $T^*$  as a function of the coupling strength  $\alpha$  obtained within NIBA for the symmetric, Ohmic spin-boson system. The full circles indicate the parameters used for the plots in Figs. 8-10. The cutoff frequency is  $\omega_c = 10 \Delta$ .

- [5] Grifoni, M., Sasseti, M. Hänggi., P., and Weiss., U. Cooperative effects in the nonlinearly driven spin-boson system. *Phys. Rev. E* **52**, 3596 (1995).
- [6] Gradshteyn, I. and Ryzhik, I. *Table of Integrals, Series, and Products* (Academic Press, New York, 7th Ed. 2007).